Synchronization of Great Subduction Megathrust Earthquakes: Insights From Scale Model Analysis

Matthias Rosenau, Illia Horenko, Fabio Corbi, Michael Rudolf, Ralf Kornhuber, Onno Oncken

▶ **To cite this version:**

Matthias Rosenau, Illia Horenko, Fabio Corbi, Michael Rudolf, Ralf Kornhuber, et al.. Synchronization of Great Subduction Megathrust Earthquakes: Insights From Scale Model Analysis. Journal of Geophysical Research : Solid Earth, 2019, 124, pp.3646-3661. 10.1029/2018JB016597 . insu-03661337

HAL Id: insu-03661337
https://insu.hal.science/insu-03661337

Submitted on 6 May 2022

HAL is a multi-disciplinary open access archive for the deposit and dissemination of scientific research documents, whether they are published or not. The documents may come from teaching and research institutions in France or abroad, or from public or private research centers.

L'archive ouverte pluridisciplinaire **HAL**, est destinée au dépôt et à la diffusion de documents scientifiques de niveau recherche, publiés ou non, émanant des établissements d'enseignement et de recherche français ou étrangers, des laboratoires publics ou privés.

Copyright

Check for updates

AGU100 ADVANCING EARTH AND SPACE SCIENCE

JGR Solid Earth

RESEARCH ARTICLE
10.1029/2018JB016597

Key Points:
- We tested geometric controls on asperity interaction and subduction earthquake recurrence behavior using seismotectonic scale modeling
- Simulated analogue earthquake sequences mimic long-term behavior of a system of two asperities coupled by static stress transfer
- The degree of synchronization and intrinsic variability is controlled by the asperity distribution

Supporting Information:
- Supporting Information S1

Correspondence to:
M. Rosenau,
rosen@gfz-potsdam.de

Citation:
Rosenau, M., Horenko, I., Corbi, F., Rudolf, M., Kornhuber, R., & Oncken, O. (2019). Synchronization of great subduction megathrust earthquakes: Insights from scale model analysis. *Journal of Geophysical Research: Solid Earth*, *124*, 3646–3661. https://doi.org/10.1029/2018JB016597

Received 22 AUG 2018
Accepted 26 FEB 2019
Accepted article online 1 MAR 2019
Published online 2 APR 2019

©2019. American Geophysical Union. All Rights Reserved.

Synchronization of Great Subduction Megathrust Earthquakes: Insights From Scale Model Analysis

Matthias Rosenau[1], Illia Horenko[2], Fabio Corbi[3,4], Michael Rudolf[1], Ralf Kornhuber[5], and Onno Oncken[1]

[1]Department of Geosystems, Helmholtz Centre Potsdam, GFZ German Research Centre for Geosciences, Potsdam, Germany, [2]Department of Mathematics and Computer Science, Università della Svizzera Italiana, Lugano, Switzerland, [3]Department of Science, Roma Tre University, Rome, Italy, [4]Géosciences Montpellier, CNRS, University of Montpellier, Montpellier, France, [5]Department of Mathematics and Computer Science, Free University Berlin, Berlin, Germany

Abstract The magnitude of great subduction megathrust earthquakes is controlled mainly by the number of adjacent asperities failing synchronously and the resulting rupture length. Here we investigate experimentally the long-term recurrence behavior of a pair of asperities coupled by static stress transfer over hundreds of seismic cycles. We statistically analyze long (c. 500 ka) time series of M8-9 analogue earthquakes simulated using a seismotectonic scale model approach with two aims: First, to constrain probabilistic measures (frequency-size distribution, variability) useful for hazard assessment and, second, to relate them with geometric observables (coseismic slip pattern, locking pattern). We find that the number of synchronized asperity failures relative to the number of individual asperity failures as well as the coefficients of variation of recurrence intervals and seismic moment scale with the logarithm of stress coupling between the asperities. Accordingly, tighter packed asperities tend to recur more periodically and with a more characteristic magnitude while more distant asperities show clustering of more variable sized events. The probability of synchronized failures seems to be controlled to first order by geometrical relations (i.e., spacing and offset of asperities). The effects of rheological properties are evident but it remains to be explored to which extent they vary in nature and how sensitive the system is to those.

1. Introduction

Giant magnitude 9 earthquakes unzip up to 1,000-km-long segments of active plate margins. Such long ruptures include failure of several asperities. Prerequisites to fail synchronously (or sequentially in short succession, i.e., within seconds) are a homogeneous high stress level along the margin (i.e., a late interseismic stage in different segments along the megathrust) and a trigger for nucleation which might be very small depending on the state of synchronization of neighboring fault segments (e.g., Scholz, 2010). Ruff (1996) introduced the idea of synchronization of the seismic cycle "clocks" in subduction zones by static stress transfer (stress coupling) leading to giant earthquakes. He developed and analyzed a simple mechanical model consisting of two frictional spring-sliders coupled by a spring as an analog of a segmented subduction zone with segments interacting by means of stress coupling (Figure 1a). He hypothesized that while individual recurrence intervals may initially be different (controlled by the individual frictional strength and spring stiffness) stress coupling may introduce variability and cause synchronization over multiple seismic cycles as mutual coseismic loading causes "clock advance" of the neighboring segments (Figure 1c). In a modern view Ruff's (1996) idea is based on static Coulomb failure stress (CFS) transfer between asperities on a fault (megathrust) bounded by an elastic medium (upper plate wedge, Figure 1b). In this model, clock advances shorten the seismic cycle of neighboring asperities gradually and trigger, if sufficiently late in the seismic cycle, synchronized events (Figure 1c). Larger clock advances (higher steps in such a figure) should potentially trigger more synchronous events as the sensitive fraction of the seismic cycle is proportionally longer. The model thus predicts that synchronization scales with stress coupling. Here we test this model and the effects of asperity distribution on stress coupling, earthquake recurrence behavior, and synchronization.

The first to model such a system realistically were Kaneko et al. (2010). They came up with a fully dynamic simulation of a pair of velocity-weakening asperities separated by a velocity-strengthening barrier. This

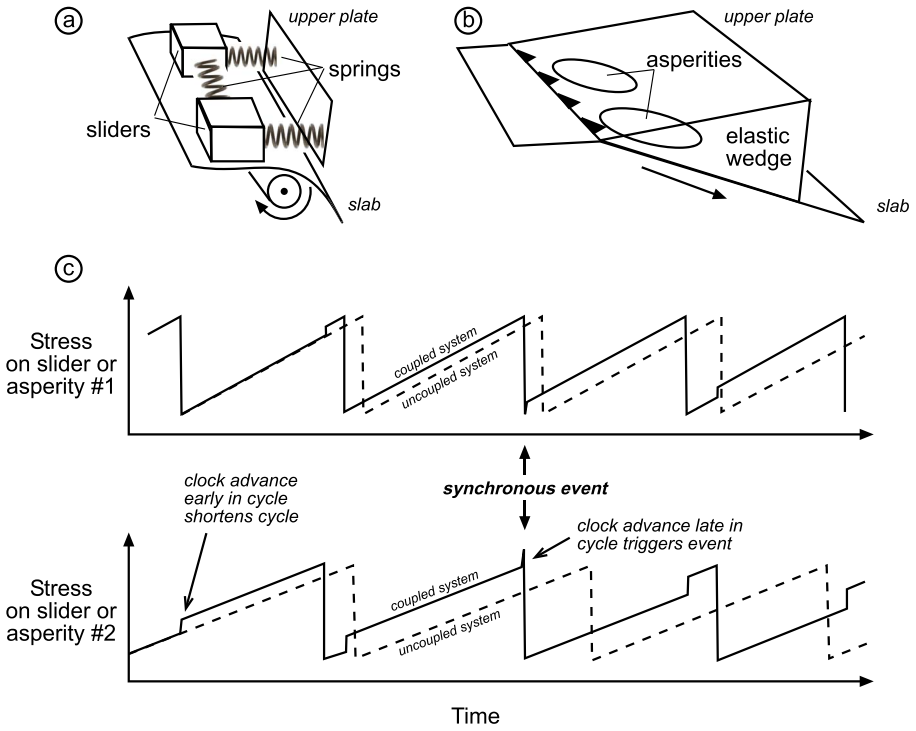

Figure 1. The concept of stress coupling and synchronization in subduction zones: (a) A system of coupled spring sliders as depicted by Ruff (1996); (b) the corresponding system of asperities coupled by static Coulomb failure stress transfer in an elastic wedge; (c) time series of stress (or strain) history (cyclic loading) of the two sliders/asperities. Note that the model predicts shortening of cycles due to clock advance early in the cycle and triggering of synchronized events by clock advance sufficiently late in the seismic cycle.

simulation demonstrated the role of the asperity distribution and frictional properties of the barrier in controlling rupture propagation across it. Because of the computational costs of such fully dynamic numerical simulations, the lengths of the simulated earthquakes where rather limited to few tens of cycles and most of the model runs were performed in 2-D.

Here we realize similar models by means of seismotectonic scale modeling (Rosenau et al., 2017) which allows a realistic simulation of comparatively long analogue earthquake sequences with up to 500 events at a rather low experiment and time cost compared to numerical simulation. We simulate a subduction zone megathrust system in an archetypical setup with two square seismogenic patches (asperities) characterized by velocity-weakening and therefore unstable stick-slip frictional behavior. The asperities are surrounded by velocity-strengthening material displaying stable creep and acting as a barrier to seismic slip. Stress coupling by means of static Coulomb failure stress (CFS) transfer is realistically implemented by the elastic wedge overlying the megathrust and quantified using elastic dislocation modeling. While frictional and elastic properties are kept constant we change the asperity distribution by varying the relative position of the two seismogenic patches along-strike and across-strike allowing us to explore the effects of variable stress coupling and strength contrasts between the two asperities.

Our study complements and extends recent analogue models by Corbi et al. (2017) who tested the geometric aspects of Kaneko et al. (2010)'s simulation using a seismotectonic scale model similar to the one we use. They were able to verify experimentally the major role of the geometric relation between the asperities in synchronization. While they were able to reproduce both the numerical results by Kaneko et al. (2010) as well as natural observations from Japan, the significance of frictional properties remained unexplored by Corbi et al. (2017).

Here we complement these studies first by providing an analogue scale model with a different set of frictional properties compared to Corbi et al. (2017) to allow testing their significance more specifically.

Second, we introduce a strength contrast between the two asperities, a factor which has not been tested experimentally or numerically so far. Third, we generated about 10 times longer analogue sequences (up to 0.5 Million years long including several hundreds of M8-M9 events) allowing a more rigorous statistical analysis and more reliable tests for statistical significance. All data underlying this study are published open access in Rosenau et al. (2019).

2. Modeling and Analysis Methods

2.1. Seismotectonic Scale Modeling of a Subduction Megathrust Setting

2.1.1. Experimental Setup and Scaling

Seismotectonic scale modeling is a cost-effective method to simulate long earthquake sequences in a fully three-dimensional, dynamic, and spatiotemporally quasi-continuous framework (e.g., Caniven et al., 2015, 2017; Corbi et al., 2013, 2017; Rosenau et al., 2009, 2017). Here we recall the basics of the approach and report modifications specific to the present study.

The experimental setup used in this study is a development from an earlier quasi-two-dimensional setup used for seismotectonic scale modeling by Rosenau et al. (2009, 2010) where the method has been explained in detail. The setup used in the current study is six times wider with respect to previous experiments and therefore truly 3-D and allows simulating along-strike analogue earthquake ruptures (e.g., Pipping et al., 2016). The experimental device consists of a glass-sided box (100 cm across-strike, 60 cm along-strike, and 50 cm deep) with a 15° dipping basal conveyer plate equipped with blades to ensure the transfer of basal stresses into the overlying material. On top of the conveyer plate an elastoplastic wedge (subduction forearc model) is set up at appropriate scale and compressed against a rigid and fixed backwall (Figure 2a).

Dynamic similarity of the laboratory scale model with the natural prototype requires the ratios of forces, which are expressed as dimensionless numbers, to be the same as in nature (Hubbert, 1937). We use the following set of dimensionless numbers to ensure similarity with respect to strength τ, gravity G, and inertia I:

1. The ratio Γ between gravitation and strength (either elastic, frictional, or viscous) is

$$\Gamma = \rho \cdot l \cdot g / \tau, \tag{1}$$

where ρ is the material density, l is a characteristic length, g is the gravitational acceleration, and τ is the elastic, frictional, or viscous strength.

2. The *Froude Number Fr* relates gravitation and inertia and is

$$Fr = v' \cdot (g \cdot l)^{-0.5}, \tag{2}$$

where v' is a characteristic coseismic velocity (e.g., rupture velocity).

3. The *Cauchy Number Ca* relates inertia and elasticity and is

$$Ca = \rho\, v'^2 / E, \tag{3}$$

where E is Young's modulus.

By keeping these dimensionless numbers the same in an experiment executed in the Earth's gravity field as in nature, the following scaling relationships are derived from equations (1) to (3):

$$\Gamma^* = \Gamma \rightarrow \left(\tau^*/\tau\right) = \left(\rho^*/\rho\right) \cdot \left(l^*/l\right), \tag{4}$$

$$Fr^* = Fr \rightarrow \left(t^*/t\right) = \left(l^*/l\right)^{0.5}, \tag{5}$$

$$Ca^* = Ca \rightarrow \left(E^*/E\right) = \left(\rho^*/\rho\right) \cdot \left(l^*/l\right)^2 \cdot \left(t/t^*\right)^2, \tag{6}$$

where "*" marks the model numbers and values. The ratios between model and natural prototype values are known as the scaling factors (Hubbert, 1937).

These scaling relationships dictate the experimental conditions and material properties (Table 1) for a given length scale and material density. The model materials (i.e., sugar, rubber, rice, silicone) used here are about

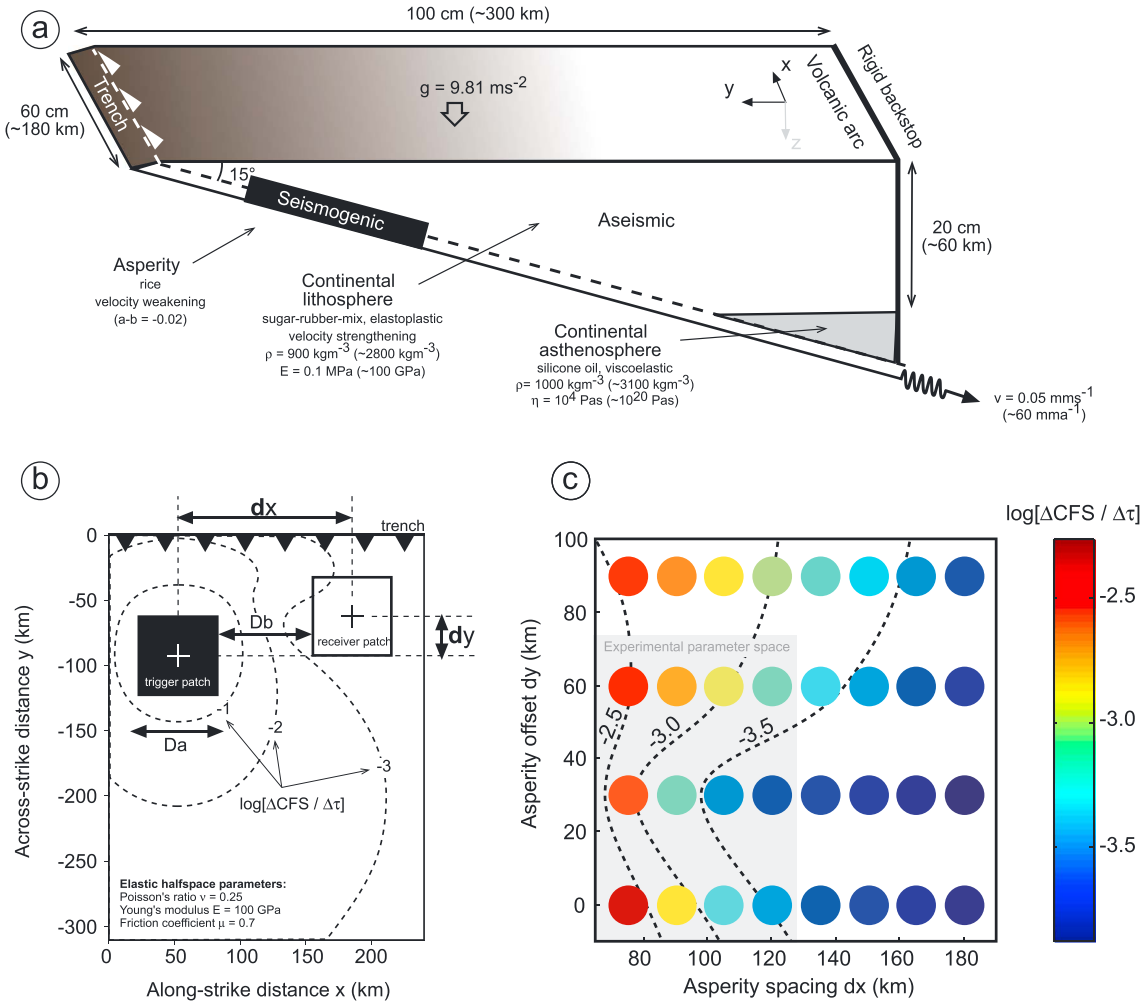

Figure 2. Seismotectonic scale model setup: (a) 3-D view of analogue model setup (cross-section corresponds to x = 50 km in (b)); (b) map-view (surface projection) of megathrust setup with calculated CFS changes ΔCFS on receiver patch (normalized to stress drop Δτ on trigger patch). Note the logarithmic fall-off with distance from the trigger asperity (see also Figure S2). Da and Db refer to the parameters used by Corbi et al. (2017). (c) Parameter space of this study: Asperity spacing (dx) and offset (dy) and corresponding stress coupling log[ΔCFS/Δτ] in color and isolines. For this plot slip is imposed on asperity #1 (trigger patch) and mean stress change calculated on asperity #2 (receiver patch). Gray shaded area corresponds to the subspace realized experimentally. Size of the asperities has not been changed in this study. CFS = Coulomb failure stress.

three times less dense than their rock equivalent and designed at a length scale $(l^*/l) = 3.3{\cdot}10^{-6}$ such that 1 cm in the scale model corresponds to 3 km in nature. According to equations (4)–(6) it follows that the scale model has to be weaker than the natural prototype by a factor $(\tau^*/\tau) = 1.1{\cdot}10^{-6}$ and should deform ~500 times slower during analogue earthquakes in order to properly scale the body forces. The corresponding coseismic time scale is $(t^*/t) = 1.8{\cdot}10^{-3}$ (i.e., 0.1 s in the lab corresponds to about a minute in nature). Because this dynamic time scale would result in unsuitable long recurrence intervals of analogue earthquakes in the laboratory and because inertial forces can be neglected during the quasi-static interevent period we scale the interseismic periods based on the *Ramberg Number* (Ramberg, 1967) which is derived from equation (1) for the viscous regime where the strength is strain rate controlled:

$$Ra = \rho{\cdot}l^2{\cdot}g/(\eta{\cdot}v), \tag{7}$$

where η is viscosity and v a characteristic interseismic velocity. According to the material properties (i.e., viscosity, density) and convergence velocity used in our experiments an interseismic time scaling factor of $1.3{\cdot}10^{-10}$ (1 s in the lab scales to ~250 years) is derived (Table 1).

Table 1
Model Parameters and Scaling Relations

	Parameters:									
	Quantity		Dimension {M,L,T}	Unit	Model		Nature		Dimensionless number	Scaling factor
Model geometry and kinematics	Length	l	L	[m]	1	cm	3	km		$3.3{\cdot}10^{-6}$
	Seismic slip	D	L	[m]	100	μm	30	m		$3.3{\cdot}10^{-6}$
	Recurrence time	T_{rec}	T	[s]	4	s	1000	a	$Ra = \rho l^2 g/(\eta v)$	$1.3{\cdot}10^{-10}$
	Rupture duration	T_{rup}	T	[s]	<0.1	s	<1	min	$Fr = v'(gl)^{-0.5}$	$1.8{\cdot}10^{-3}$
	Convergence velocity	v	L/T	[m/s]	50	μm/s	60	mm/a		$2.6{\cdot}10^{4}$
	Rupture velocity	v'	L/T	[m/s]	5	m/s	3	km/s	$Ca = \rho v'^2/E$	$1.8{\cdot}10^{-3}$
	Gravitational acceleration	g	L/T^2	[m/s^2]	9.81	m/s^2	9.81	m/s^2		1
	Coseismic acceleration	a'	L/T^2	[m/s^2]	0.6	m/s^2	0.6	m/s^2		1
Material properties	Friction coefficient[a]	μ			0.7		0.7			1
	Friction rate parameter	a-b			+/−0.02		+/−0.02			1
	Cohesion	C	M/LT^2	[Pa]	10	Pa	100	MPa		$1.1{\cdot}10^{-6}$
	Young's modulus	E	M/LT^2	[Pa]	100	kPa	100	GPa		$1.1{\cdot}10^{-6}$
	Viscosity	η	M/LT	[Pas]	$2{*}10^4$	Pas	10^{20}	Pas		$1.4{\cdot}10^{-16}$
	Density	ρ	M/L^3	[kg/m^3]	900	kg/m^3	2800	kg/m^3		$3.3{\cdot}10^{-1}$
Forces	Gravitation	G	ML/T^2	[N]						$1.2{\cdot}10^{-17}$
	Inertia	I	ML/T^2	[N]						$1.2{\cdot}10^{-17}$
Strength & energy	Strength[b]	τ	M/LT^2	[Pa]	500	Pa	500	MPa	$\Gamma = \rho l g/\tau$	$1.1{\cdot}10^{-6}$
	Stress drop	$\Delta\tau$	M/LT^2	[Pa]	100	Pa	100	MPa		$1.1{\cdot}10^{-6}$
	Seismic moment	M_0	ML^2/T^2	[Nm]	1	Nm	$3{\cdot}10^{22}$	Nm		$4.0{\cdot}10^{-23}$

Note. M = Mass; L = Length; T = Time.
[a]Interseismic. [b]At seismogenic depth.

Note that scale models embody strong simplifications with respect to the natural prototype. Therefore, their application may be limited to those aspects realistically implemented (i.e., frictional behavior, elastic loading, etc.). See Rosenau et al. (2017) for a review of the seismotectonic scale modeling approach.

2.1.2. Scale Model Configuration and Material Properties

The generalized subduction zone model presented here is analogous to a 300-km-wide and 180-km-long forearc section from the trench to the volcanic arc (Figure 2a). The scale model is made up of a granular wedge of an elastic-frictional plastic (elastoplastic) mixture of EPDM (Ethylene-propylene-diene-monomer) rubber pellets with refined sugar and flavored rice representing the brittle forearc lithosphere. The wedge overlies PDMS (Polydimethyl-siloxane) silicone oil representing the viscoelastic asthenosphere. We generalize the natural subduction geometry by considering a planar, 15°-dipping megathrust between an upper plate made up of ~60-km-thick lithosphere and ~20-km-thick asthenosphere below the arc and an oceanic plate. The latter is represented by a conveyer plate pulled constantly via a spring-loaded thrust pad at 50 μm/s simulating plate convergence at a long-term rate of about 60 mm/a in nature.

The model megathrust is defined by a few millimeters wide granular shear zone which forms at the base of the wedge (analog to a "subduction channel," Shreve & Cloos, 1986). It is characterized by rate- and state-dependent frictional behavior similar to nature (Scholz, 1998). In particular, it includes two square, velocity-weakening patches of basal area A (20 × 20 cm ~ 60 × 60 km) displaying stick-slip deformation and mimicking a pair of seismogenic asperities separated by a velocity-strengthening, aseismic barrier. The seismogenic depth range is limited between ~5 and 40 km as constrained by geothermal models (e.g., Oleskevich et al., 1999) and geodetic inversions (e.g., Li et al., 2015) of natural prototypes. The two stick-slip patches (asperities) are actually thin cuboid volumes of flavored rice embedded into the wedge material during the manual sieving procedure. During an experiment the cuboids are sheared into trapezoids without significant geometric change of the actual shear plane. The friction rate-parameter a-b within the asperities is approximately −0.02 (Rosenau et al., 2009). The wedge material including the barrier separating the two asperities as well as updip and downdip regions of the asperities are characterized by "aseismic" slip or stable sliding (creep) controlled by the velocity-strengthening behavior (a-b ~ +0.02, Rosenau et al., 2009) of frictional slip in the sugar-EPDM mixture. A viscous wedge made of PDMS (Polydimethylsiloxane) silicone oil (Korasilon G30M) corresponds to the mantle wedge in nature. Material properties of this seismotectonic

scale model approach have been documented in detail in Rosenau et al. (2009, 2010) and Rudolf et al. (2016) and are reported in Table 1.

The two asperities have an along subduction zone strike center-to-center distance (hereafter called spacing) dx (25, 30, 35, 40 cm ~ 75, 90, 105, 120 km in nature) and a relative shift across subduction zone strike (hereafter called offset) dy (0, 10, 20 cm ~ 0, 30, 60 km in nature, Figure 2b). This allows exploring the effects of asperity distribution on stress coupling (as defined below in section 2.2.2) as well as strength contrast. We define the latter as the shear strength of the weaker (shallower) patch (asperity #2) relative to the stronger (deeper) patch (asperity #1):

$$\text{Strength contrast} = \tau_2/\tau_1. \quad (8)$$

Strength contrast therefore ranges theoretically from close to 0 to 1. Note the somewhat counterintuitive effect that low strength contrasts are reflected by high τ_2/τ_1 values. In total 12 configurations of asperity distributions have been realized in which we vary the strength contrast from 0.6 to 1.0 and the stress coupling from a few ppm to few percent (Figure 2c). The experimental runs took place under normal gravity conditions and in a dry room climate (22–23 °C, 30–40% humidity).

2.1.3. Experimental Monitoring and Strain Analysis

For strain analysis of the evolving model wedges we use an optical image acquisition and correlation system (particle image velocimetry, PIV StrainMaster by LaVision, Germany, see Adam et al., 2005; Rosenau et al., 2009, 2010, 2017, for applications in analogue tectonic and earthquake modeling).

During an experiment, the locations of particles on the model surface (i.e., within the *x*-*y* plane of the model, Figure 2) are recorded by sequential 11 MPx digital images of a 14-bit monochrome charge-coupled device camera acquired at a frequency of 10 Hz. The *x*-*y* displacement vector field between successive images is then determined by cross-correlation of textural differences (i.e., gray values) formed by groups of particles using a Fast Fourier Transform algorithm. The spatial resolution of the final displacement vector grid is ~3 mm or about 1 km in nature. For each grid-cell, an average horizontal displacement vector is determined at micrometer precision (~decimeter scale in nature). This allows for observing episodic surface deformation events corresponding to earthquakes of moment magnitude $M_w > 8$. Analogue earthquakes are characterized by episodic, usually more than one order-of-magnitude increased strain rates and a change in polarity of the wedge deformation from "landward" motion (in negative y-direction) and shortening of the wedge during the interseismic stage to "trenchward" motion and extension of the wedge during the coseismic stage (Figure 3). Earthquakes typically occur within a 0.1-s time interval, that is, are captured by a single image.

2.2. Elastic Dislocation Modeling

We use elastic dislocation modeling following Okada (1985, 1992) for coseismic slip inversion and static Coulomb failure stress (CFS) transfer calculation. We employ the Matlab-based software package "Coulomb" by Toda et al. (2011). The model setup for elastic modeling uses the up-scaled geometry of the analogue model and according prototype material properties (see Figure 2b).

2.2.1. Slip Inversion

Surface deformation during analogue earthquakes as captured by PIV is converted into coseismic slip along the megathrust using inversion factors derived by forward elastic dislocation modeling. Accordingly, we find the factors relating horizontal surface deformation in the trenchward (y-) direction above the dislocation center to dislocation slip D at depth to range between 0.2 and 0.5 depending nonlinearly on the trench distance (or depth) of the dislocation (Figure S1). Shallow dislocations show larger factors, that is, are less attenuated. We do not aim at a formal inversion or distributed slip modeling. Instead, we consider here mean coseismic surface displacement over the projected surface area of the seismogenic patch to be a valuable proxy for mean coseismic slip over the asperity at depth.

2.2.2. Stress Coupling

For quantifying the interaction by means of stress coupling between the asperities we follow the principles of static CFS transfer modeling as established by King et al. (1994), Toda and Stein (2002), and Lin and Stein (2004).

The model setup for CFS modeling is such that we impose uniform thrust slip on a trigger patch and average the predicted CFS change (ΔCFS) for thrust faulting on the receiver patch (e.g., Figures 2b, 2c, and S2). To

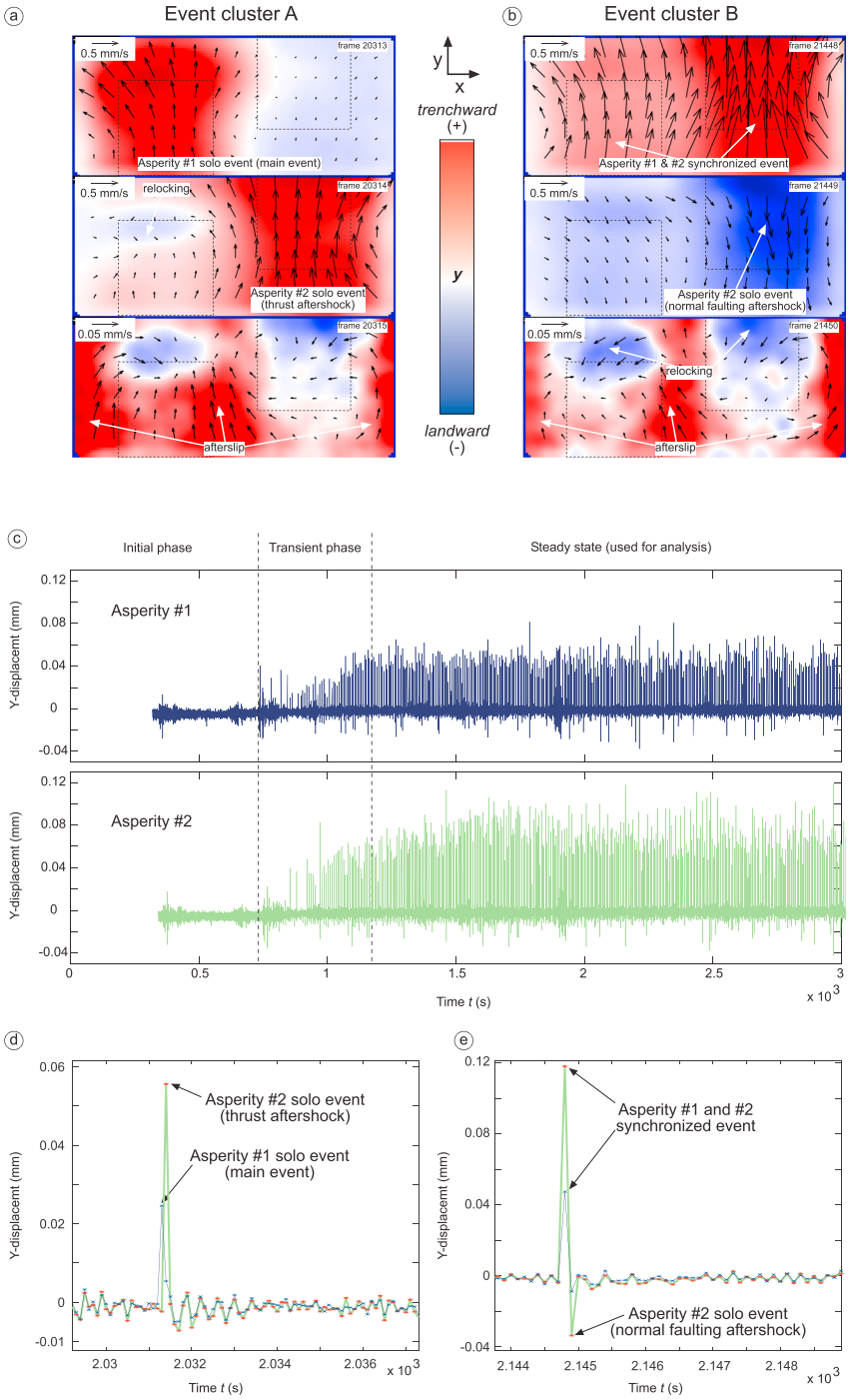

Figure 3. Example of incremental surface deformation (velocity) pattern on top of the asperities in experiment #15 (dx = 30 km, dy = 10 km) characterized by an intermediate stress coupling ($\log[\Delta CFS/\Delta\tau] = -2.65$) and strength contrast ($\tau_2/\tau_1 = 0.77$),: (a) Event clusters example A consisting of two solo events (main event in asperity #1 and aftershock in asperity #2) followed by afterslip and relocking (each velocity field corresponds to 0.1 s experimental time). (b) Event cluster example B consiting of a synchronized event (in both asperities) followed by a normal event in asperity #2, relocking and afterslip. Note the different vector scale for coseismic (upper, middle panel) and postseismic phases. Colors are scaled to the maximum velocity in each panel (red = surface displacement toward trench (y-direction), white = 0, blue = away from the trench/landward). The thin stippled squares indicate the surface projection of the asperities. (c) Time series of incremental y-displacement averaged over the surface projected area of asperity 1 (top panel) and asperity 2 (bottom panel). Note the evolution from an initial "aseismic stage" toward a "seismic" steady state with a transient stage in between. We used only data from the seismic steady state for further analysis. Note also the asymmetry in displacements above shallow and deep asperity which is related to the free-surface effect. (d and e) Zoom into incremental surface displacement time series of the two event clusters A and B, respectively.

derive at a dimensionless parameter describing the asperities' interaction ("stress coupling") we normalize ΔCFS on the receiver patch to static stress drop on the trigger patch.

$$\text{Stress coupling} = \Delta\text{CFS}/\Delta\tau. \tag{9}$$

We calculate the static stress drop Δτ as proportional to the product of strain (i.e., mean slip D over patch dimension $A^{1/2}$) and Young's modulus E (e.g. Lay & Wallace, 1995):

$$\Delta\tau = S{\cdot}E{\cdot}D/A^{1/2}. \tag{10}$$

Because of the uncertainties in natural material properties and actual rupture geometry, we use a Young's modulus E of 100 GPa and a shape factor S, which is close to one in nature, of 1 for calculation. In the presence of a strength contrast we do this calculation for both cases where either the deep or shallow asperity act as a trigger patch and average the resulting stress changes on the receiver patches. Note that stress coupling as defined here is a parameter independent of the actual slip on the trigger patch.

In the present setup stress coupling is in the order of less than a ppm up to 1% similar to nature (Figures 2b, 2c, and S2). Stress coupling falls off exponentially with distance and varies nonlinearly across-strike of the megathrust as a function of asperity spacing (dx) and offset (dy).

2.3. Surface Deformation Time Series Analysis: Event Detection and Classification

Experimental time series of surface deformation consist of typically a sequence of 30,000 images and corresponding incremental displacement vector fields for each experiment. To detect analogue earthquakes from such a big data set we usually rely on computational algorithms sensitive to accelerations validated by visual inspection. However, because of experimental noise such a kinematic approach based on thresholding velocity usually has a high detection limit. Instead of thresholding velocities to detect earthquakes we here employ a numerical time series analysis technique developed in computational statistics. This allows us to automatically detect and classify events which can be below the detection threshold of classical kinematic approaches.

As input we use the surface deformation time series at the orginal frequency of 10 Hz. In particular we use across-strike (y-) displacements averaged over the surface projected area of the two individual asperities (Figure 3). Those data typically show an initial aseismic phase without much activity reflecting stress buildup and reorganization within the scale model (Figure 3c) followed by a transient phase of increasing activity leading over into a "seismic" steady state. We use observations from this steady state for further analysis.

To analyze the obtained experimental time series, we deploy a nonparametric time series analysis methodology called Finite-Element-Method with Bounded Variation of model parameters (FEM-BV; Horenko, 2009, 2010; Metzner et al., 2012). Although it is computationally more expensive than the common methods, FEM-BV has several important conceptual advantages that were recently illustrated for various time series analysis applications in geosciences (Franzke et al., 2015; Kaiser et al., 2015; O'Kane et al., 2016; Risbey et al., 2015; Vercauteren & Klein, 2015). This nonparametric method is automatized, does not rely on any tunable user-defined parameters (like thresholds values for the event identification) and allows to go beyond strong parametric assumptions (like linearity, Gauss or Poisson distribution assumptions for observed densities, stationarity, or Markovianity)—assumptions that are a constitutive part of the more common statistical time series analysis approaches like multilinear regression, Hidden Markov Models, or clustering methods (e.g., Shearer & Stark, 2012). Going beyond these assumptions is especially important since analyzed data exhibits a strong regime-transition behavior, is nonstationary, non-Markovian, and non-Gaussian in the regimes. Moreover, defining ad hoc threshold values for the events could potentially introduce a user-defined bias. We refer to Metzner et al. (2012) for mathematical/statistical details of the FEM-BV methodology—as well as for its computational comparison with more common time series analysis methodologies.

The result of this analysis is a catalogue of analogue earthquake events classified into "solo" events which occur either in asperity #1 (deep/left with respect to Figure 2b) or in asperity #2 (right/shallow) versus "synchronized" (double) events where both asperities fail synchronously within one time frame (0.1 s; Figure 4a and data publication Rosenau et al., 2019). A further classification of solo events is based on interevent time. We refer to two events which occur separately in the two asperities within successive frames (i.e., $T_{rec} = 0.1$ s)

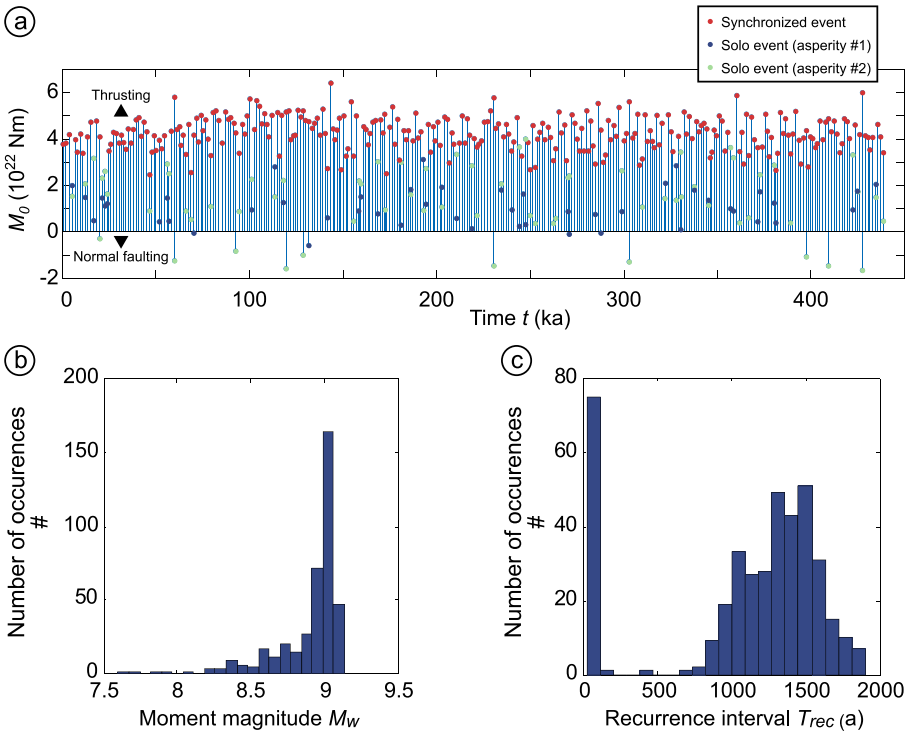

Figure 4. Example of an earthquake sequence simulated in experiment #15 (dx = 30 km, dy = 10 km) characterized by an intermediate stress coupling ($\log[\Delta CFS/\Delta\tau] = -2.65$) and strength contrast ($\tau_2/\tau_1 = 0.77$), (all parameters scaled to nature): (a) event catalogue as derived by the numerical FEM-BV approach. Positive and negative seismic moments correspond to thrusting and normal faulting, respectively. The events are color coded to differentiate synchronized events (red) from solo events in the two patches (blue and green). (b) PDF of moment magnitude M_w. (c) PDF of recurrence interval T_{rec}. The peak at low recurrence intervals represent clustered events interpreted as aftershocks. See appendix Figure S4 for PDFs of all experiments. PDF = probability density function.

as "clustered" events, with the first being the "main event" and the second event being an "aftershock." All events can also be divided based on their faulting mechanism (i.e., thrust versus normal faulting), however, it appears that normal faulting is only observed in aftershocks. A flow-chart describing the event classification is shown in Figure S3.

2.4. Statistical Analysis of Analogue Earthquake Sequences

Here we are ultimately interested in the control of extrinsic parameters (stress coupling and strength contrast) on the variability of earthquake sequences in general, and the probability of synchronized events in special. A simple measure of probability of any class of events used by earlier studies (e.g., Corbi et al., 2017; Kaneko et al., 2010) is the number of events of that class relative to the total number of events. Based on the long sequences of analogue earthquakes in our synthetic catalogs we can go, however, beyond this simple approach and explore the intrinsic (stochastic) and extrinsic (parameter-controlled) variability of the frequency-size distributions by means of univariate and bivariate statistics.

In particular, we use probability density functions (PDFs) and their coefficients of variation (CV) to describe the intrinsic variability of individual earthquake sequences. PDFs of moment magnitudes M_w (Figures 4b and S4) mimic the high-magnitude (M8+) end of natural frequency-size relationships while PDFs of the seismic moment M_0 and the recurrence interval T_{rec} (Figures 4c and S4) and their CV are used to differentiate between periodic and aperiodic (e.g., random, clustered) occurrence of events.

The CV is defined as the standard deviation σ of a data population normalized to their mean value M:

$$\mathrm{CV} = \sigma/\mathrm{M} \tag{11}$$

and serve as a first-order proxy for the intrinsic variability of the frequency-size distributions in individual earthquake sequences: A CV of 1 characterizes a random distribution of recurrence intervals or

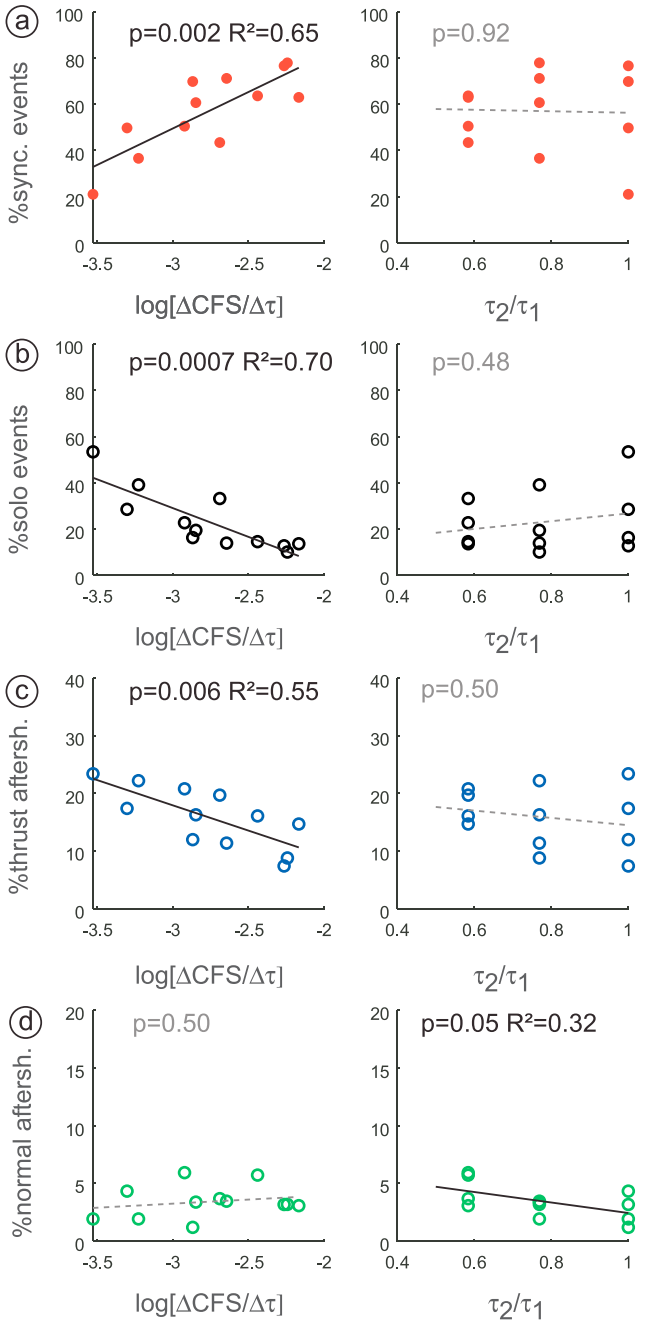

Figure 5. Percentage of individual classes of events versus stress coupling (ΔCFS/Δτ, left column) and strength contrast (τ2/ τ1, right column): (a) synchronized events, (b) solo events, (c) thrust aftershocks, (d) normal aftershocks. Linear regressions with $p < 0.05$ are considered significant correlations, those with $p = 0.05$–0.1 marginal. See Table S2 for all p and R^2 values and text for interpretation of the correlations. CFS = Coulomb failure stress.

magnitudes. A CV <1 suggests a (quasi-) periodic recurrence or a characteristic magnitude of events. A CV >1 is characteristic of clustering in time or a dominance in small magnitudes (e.g., Kuehn et al., 2008; Rosenau & Oncken, 2009).

To test the control of extrinsic parameters (stress coupling and strength contrast) on recurrence behavior we finally analyzed the correlation of mean values and of CVs of M_0 and T_{rec} with (the logarithm of) stress coupling and with strength contrast by means of linear regression. We use probability (p) values and coefficients of determination (R^2) to describe the goodness-of-fit of, and the extrinsic variability explained by, (log)linear regression models, respectively. A p value threshold of 0.05 is used to reject or accept the (log)linear model. P values between 0.05 and 0.1 are considered marginal.

3. Experimental Observations and Interpretations

3.1. Seismic Performance of the Scale Model

All experiments followed a consistent characteristic evolution from aseismic to seismic behavior (Figure 3c): An early initial phase (about minutes 0–15) of aseismic deformation is dominated by distributed wedge shortening and minor thickening and followed by a transient phase of increasing seismicity (about minutes 15–20). After about 20 min the wedge is in a steady state characterized by stationary time series of cyclic surface accelerations reflecting analogue earthquakes. The seismic evolution reflects the progression of the model deformation from dominantly plastic to dominantly elastic (Rosenau & Oncken, 2009).

A typical earthquake catalogue simulated by our scale model in the steady state consist of up to 500 events of moment magnitude M_w 8–9 which occur over a time-period of about 500 ka in nature (Figure 4a). M8 events usually involve only one asperity while a synchronized failure of both asperities typically results in M9 events. Analogue earthquakes are always followed by afterslip lasting for not more than one frame (0.1 s or ~25 years in nature) surrounding the asperities (Figures 3a and 3b). Generally, the shallow asperity generates more surface displacement than the deep one: this is related to static effects as predicted by elastic dislocation modeling (Figure S1). The picture inverts when the correction for depth of dislocation is applied. In that case, deeper asperities show larger slip. This is consistent with higher loads causing higher frictional strength at greater depth as predicted by Mohr-Coulomb theory. As a consequence, the deeper asperities are mechanically stronger, fail at higher shear stresses and are therefore able to accumulate more slip deficit in the correspondingly longer interseismic periods compared to the shallow asperities.

A minority of aftershocks are relatively small normal faulting events. We interpret those as a result of dynamic overshoot during the preceding thrust event. Normal events occur almost exclusively in the shallow asperity. We include those rare normal events in our analysis since they represent an integral part of the long-term slip budget. Accordingly, they show up with a negative seismic moment in Figure 4a.

3.2. Event Probability

When analyzing the probability of occurrence of the different classes of events as a function of stress coupling ΔCFS/Δτ and strength contrast τ2/τ1 a clear picture emerges (Figure 5 and Table S1). Accordingly,

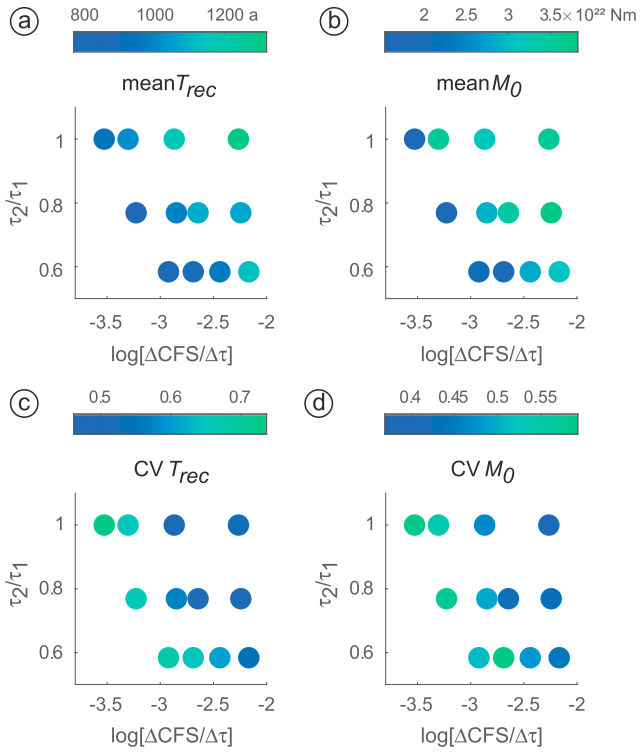

Figure 6. Visualization of the variation of mean recurrence interval and its CV (a and c) and mean seismic moment and its CV (b and d) in the parameters space, that is, with stress coupling (ΔCFS/Δτ) and strength contrast (τ2/τ1). See Table S2 for linear regression analysis results. CFS = Coulomb failure stress; CV = coefficient of variation.

synchronized events increase in number from 20% to 80% of total events as stress coupling increases by two orders of magnitude (from less than a ppm up to a percent, Figure 5a). Consistently, solo events decrease (Figure 5b). This testifies a higher degree of synchronization in strongly coupled systems. Regarding clustered events, only pairs with thrust aftershocks show a clear correlation with stress coupling (Figure 5c). Those clustered pairs with normal faulting aftershocks show no clear correlation with stress coupling but a negative correlation with τ2/τ1 (Figure 5d). This is consistent with overshoots occurring preferentially in shallow regions of the wedge. All other classes of events show, however, no significant correlation with strength contrast. An apparent increase of the range of proportions of individual events with τ2/τ1 reflects the systematically wider range in stress coupling realized for models with high τ2/τ1 (e.g., Figure 6).

3.3. Frequency-Size Distributions

Frequency-size distributions of simulated earthquakes share similar shapes. The probability density functions (PDFs) of moment magnitude are generally skewed negatively (toward the left) and very peaked as exemplified in Figure 4b. The PDFs of recurrence intervals are generally bimodal, characterized by a peak at short periods (0.1 s or 25 years) and a quasi-normally distributed peak around the mean recurrence interval of large events (at ~1000-1500 years) as exemplified in Figure 4c.

3.4. Intrinsic and Extrinsic Variability

Plotting mean recurrence intervals and mean seismic moments of all events in individual models and their variability in terms of CV into the parameter space (Figure 6) shows the following: Mean recurrence interval and seismic moment both increase with an increase in stress coupling (Figures 6a and 6b). At the same time their CVs decrease (Figures 6c and 6d).

We interpret this correlation of M_0 and T_{rec} with stress coupling as reflecting a dynamic interaction causing higher slip in case of more strongly coupled asperities. Larger slip per event consistently lengthens the interseismic period resulting in longer recurrence intervals in order to keep the long-term seismic slip rate constant. The increase in magnitude seems also to regulate the seismic cycle, decreasing the CV of M_0 and T_{rec} by about 20%.

A weak positive correlation seems to exist between T_{rec} and strength contrast but the p value is marginal ($p = 0.1$, Table S1) and only about one fourth of the variability is explained by extrinsic control ($R^2 = 0.25$, Table S1). Accordingly, earthquake frequency increases as the weak asperity becomes weaker. We interpret this as being the behavior predicted by Ruff (1996) where the weaker asperity, which has intrinsically shorter recurrence times, causes clock advance of the stronger asperity, which has intrinsically longer recurrence intervals. No correlation exists between M_0 as well as the associated CVs with strength contrast.

The correlations of M_0 and T_{rec} with ΔCFS/Δτ are replotted in Figure 7 with a differentiation between all events and synchronized events only to explore the effects of stress coupling on intrinsic and extrinsic variability in more detail. Consistently, consideration of only synchronized events, which are generally larger than solo events, increases mean seismic moment and mean recurrence interval and decreases the associated CVs.

More interestingly, however, is the observation that the trends differ for the two groups of events: For example, the positive correlation of T_{rec} with stress coupling observed for all events is inverted to a negative correlation if only synchronized events are considered (Figure 7a). This is the result of synchronized events being systematically rarer in more weakly coupled systems as has been predicted by Ruff (1996). At the same time, recurrence intervals of synchronized events are more sensitive to stress coupling having a higher $R^2 = 0.44$ than the recurrence intervals of all events ($R^2 = 0.29$). In fact, synchronized events recur almost

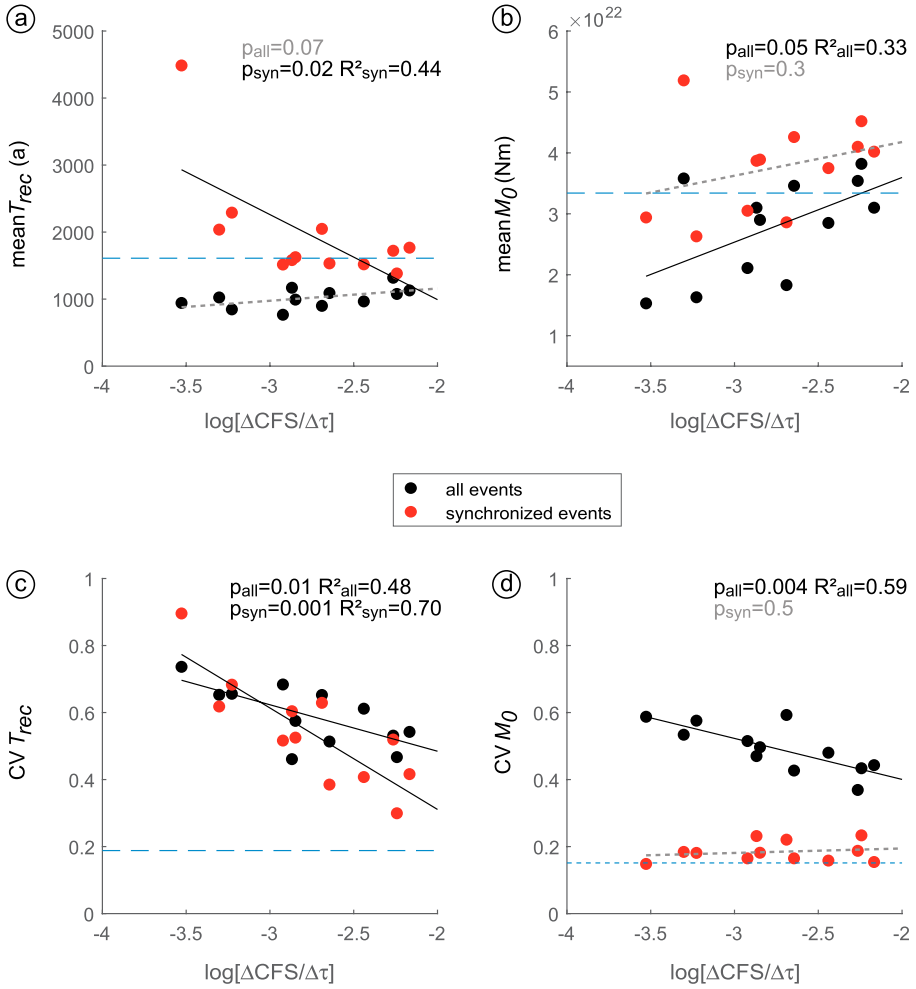

Figure 7. Bivariate plots of the most significant trends from Figure 6 with two classes of events differentiated (all events = black dots, synchronized events = red dots): Variation of mean recurrence interval T_{rec} (a) and its CV (c) as well as mean seismic moment M_0 (b) and its CV (d) with stress coupling (ΔCFS/Δτ). Linear regressions with $p < 0.05$ are considered significant correlations, those with $p = 0.05$–0.1 marginal. See Table S2 for all p and R^2 values and text for interpretation of the correlations. Horizontal stippled line indicates the corresponding value in an experiment with a single asperity (Rosenau et al., 2017) for reference. CFS = Coulomb failure stress; CV = coefficient of variation.

randomly for weakly coupled systems (CVT_{rec}~0.9) and periodically for strongly coupled systems (CVT_{rec}~0.3). On the other side, the magnitudes' variability is minimized for synchronized events as compared to all events (CV 0.2 vs 0.4–0.6) and independent of stress coupling ($p = 0.5$).

In conclusion, our analysis indicates that stress coupling has the effect of causing more periodic, characteristic events. Compared to a reference experiment with a single asperity by Rosenau et al. (2017), however, any system of two asperities realized here shows a more complex recurrence behavior indicated by generally more frequent and smaller events (lower T_{rec} and M_0) and significantly higher CVs (Figure 7).

4. Discussion

4.1. Relation Between Asperity Distribution and Recurrence Behavior: A Characteristic Length Scale in Nature?

Based on experimentally simulated long subduction earthquake records we are able to shed light on the control of asperity distribution on the variability of subduction earthquakes in terms of magnitude and recurrence intervals. Rosenau et al. (2017) showed that the transition from a single asperity to two weakly coupled asperities involves a principle change from periodic (recurrence interval's CV ~0.2) toward more randomly occurring earthquakes (CV ~1). This is consistent with spring-slider models suggesting a single

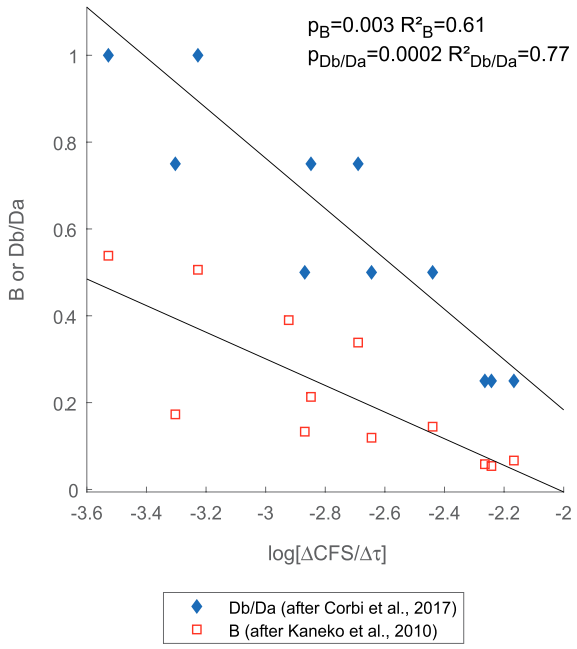

Figure 8. Correlation of stress coupling (ΔCFS/Δτ) with existing proxies of barrier efficiency B (after Kaneko et al., 2010) and Db/Da (after Corbi et al., 2017). The good correlations verifies that the three different proxies are interoperable. Linear regressions with $p < 0.05$ are considered significant correlations, those with $p = 0.05$–0.1 marginal. See Table S2 for all p and R^2 values and text for interpretation of the correlations. CFS = Coulomb failure stress.

isolated spring-slider system to be periodic while a coupled pair of spring-sliders shows a complex behavior (e.g., Ruff, 1996). The system simulated here shows a strong correlation between the stress coupling (controlled by asperity distribution) and recurrence variability increasing from 0.3 to 1 as stress coupling decreases (Figure 7c). At the same time earthquakes become more variable in magnitude as stress coupling decreases suggesting a causal link between characteristic earthquake behavior and asperity distribution.

The range in CVs in recurrence intervals spans a considerable larger range than what is seen in natural examples which is usually characterized by a CV <0.4. For example, the Holocene tsunami record offshore western North America suggest that great M_w 9 Cascadia subduction zone earthquakes have occurred about every 500 to 600 years during the past 10 kyr (Goldfinger et al., 2003) with a CV of 0.36–0.39 (Sykes & Menke, 2006). For the Nankai trough, Sykes and Menke (2006) report a CV of 0.26–0.27. In the Northern Chile-Southern Peru seismic gap which last broke in 1877 (M_w 8.8) the reported historical recurrence interval for the past 500 years has been estimated at 111 ± 33 years (Comte & Pardo, 1991) resulting in a CV of 0.3. Similarly, in southern Chile, in the area of the great 1960 and 2010 earthquakes, leveling and dating of Holocene strandlines by Bookhagen et al. (2006) suggests that great earthquakes have occurred every 180 ± 65 years over the last 3 to 4 kyr, from which a CV = 0.36 can be calculated. Clearly the regularity of great megathrust earthquakes implied by their low CV breaks down below about M_w 8. However, b-values significantly below 1 for M_w 5–8 earthquakes in many subduction zone (e.g., Bilek & Lay, 2018) suggest a nonrandom behavior also at smaller magnitude.

Although the natural data base is limited, this rather narrow range of low CVs and b-values in nature in combination with the here suggested causal link between regularity and asperity distribution let us speculate that there might be a characteristic length scale in the asperity distribution in nature. In our models a CV <0.4 in recurrence intervals is reached only by the narrow configurations where barriers between asperities are significantly smaller than the asperities themselves. Such a narrow asperity configuration can be found for example in the region of the 1960 and 2010 Chile earthquakes (Moreno et al., 2009, 2010, 2011). More examples can be found, for example, in Hayes (2017) finite fault model data base, however, a rigorous review of natural examples with respect to this aspect is beyond the scope of this paper.

4.2. Predicting Asperity Interaction: Toward Proxies for Barrier Efficiency

We simulated long time series of analog subduction megathrust earthquakes in order to constrain the recurrence pattern of a simple system with two asperities coupled by static stress transfer. Similar experiments (Corbi et al., 2017) and numerical simulations (Kaneko et al., 2010) have been carried out to find the critical parameters controlling the probability of a rupture bridging the barrier and causing a synchronized failure of the asperities. We here add experimental data representing a different set of material parameters and geometries which allows testing the existing concepts and to identify the minimum set of parameters needed.

Kaneko et al. (2010) suggested a set of parameters combined in a proxy for barrier efficiency called B. B is the ratio of the stress increase required to bridge the barrier to the coseismic stress drop. B included parameters which are directly and indirectly (involving assumptions) observable in nature (geometric, kinematic, dynamic, and friction parameters). Given the complexity of B and the uncertainty in the choice of some of the parameters included (e.g., frictional parameters), Corbi et al. (2017) aimed at a more simple proxy based solely on first-order geometric relationships easy to observe in nature, that is, the barrier-to-asperity length ratio Db/Da. With respect to these two proxies, we consider the stress coupling as defined here as a proxy for barrier efficiency of intermediate complexity. Similar to Db/Da, stress coupling can be inferred primarily from geometric observations (size and location of asperities).

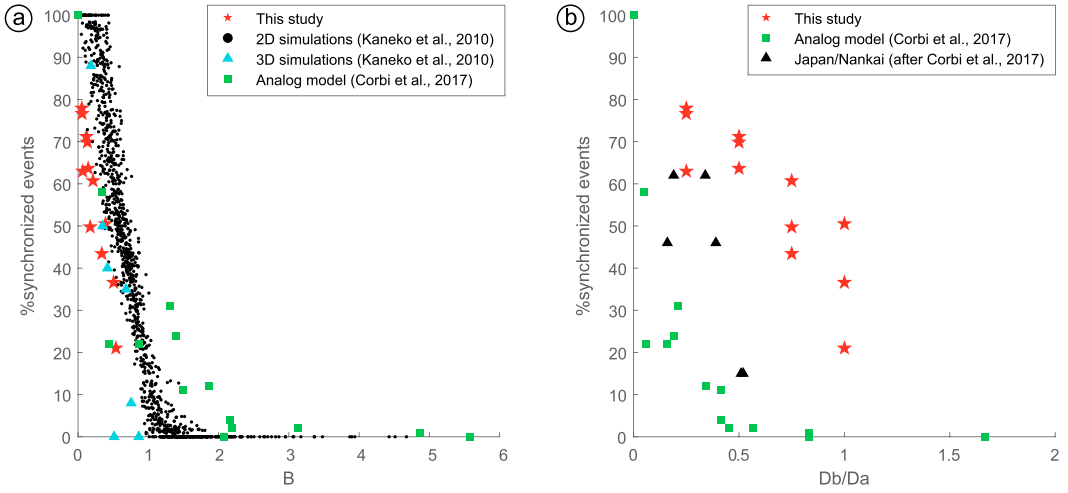

Figure 9. Percentage of synchronized events from various sources as a function of existing proxies for barrier efficiency: (a) B (after Kaneko et al., 2010), (b) Db/Da (after Corbi et al., 2017). Note the collapse of experimental, natural, and numerical simulation data in (a) indicating its universal nature. Parallel offset trends in (b) are interpreted as due to differences in frictional properties between the experiments and nature which are not taken into account in the parameter Db/Da.

In Figure 8 we compare the three proxies based on the setup presented in this study. Obviously, there is a good correlation between stress coupling, B, and Db/Da. Db/Da seems slightly more sensitive to stress coupling than B as suggested by its steeper slope in this plot. In any case, a correlation coefficient (R^2) of 0.6 to 0.8 suggests general interoperability of the three proxies.

Figure 9 shows the collapse of existing experimental and numerical as well as real world data from the Nankai subduction zone (Corbi et al., 2017) in a plot of percentage of synchronized events versus B. In contrast, plotting those data against Db/Da separates the data into roughly parallel trends. Because the data used represent a wide spectrum of geometrical and frictional parameters, the collapse indicates the universal nature of the proxy B for anticipating the probability (i.e. percentage) of synchronized events.

On the other hand, the systematic offset trends suggest that while Db/Da seems to have a strong control on synchronization, material properties cannot be neglected. For instance, it appears that the setup used in the present study generates synchronized events more easily. While for the experiments by Corbi et al. (2017) and the natural example a threshold for synchronized events at Db/Da of 0.5 emerges, in the experiments presented here this threshold is significantly higher (>1). This suggests that the barrier in the Corbi et al. (2017) experiments as well as in the Nankai area are mechanically more effective than in our setup.

We conclude that for the moment, the full complexity of the proxy B by Kaneko et al. (2010) is needed to account for the variability of mechanical parameters present in the experiments. To which extent these parameters vary in nature and therefore control the threshold value of Db/Da remains to be explored.

5. Conclusions

Based on experiments with seismotectonic scale models generating long time series of analog subduction megathrust earthquakes we explored the process of interaction and synchronization of two velocity-weakening asperities separated by a velocity-strengthening barrier. We found the following:

1. Synchronization of asperities is controlled by the static Coulomb failure stress (CFS) transfer, here quantified by the stress coupling $\Delta CFS/\Delta\tau$. Accordingly, the percentage of synchronized events scales with the logarithm of (normalized) CFS change.
2. A strength contrast between the two asperities has no significant effect on synchronization but decreases the recurrence interval of synchronized events because the weaker asperity dictates the system's recurrence intervals.

3. Analogue earthquakes in strongly coupled systems (narrower asperity distribution) recur more periodically and with a more characteristic magnitude than in weakly coupled systems.
4. A narrow asperity distribution might be typical for natural subduction zones characterized by quasi-periodic recurrence.

Three proxies for the barrier efficiency, B (Kaneko et al., 2010), Db/Da (Corbi et al., 2017), and the newly defined stress coupling $\Delta CFS/\Delta\tau$ have been cross-validated and tested for applicability:

1. Db/Da is the most simple and easiest to apply proxy and incorporates the most sensitive parameters to work first-order. It relies on geometries which—if they are stationary over multiple seismic cycles—we are able to constrain using interseismic locking and paleoseismological observations.
2. B is the most universal proxy and it captures the physics—but several parameters are needed and not well constrained or uncertain in nature.
3. $\Delta CFS/\Delta\tau$ is of intermediate complexity and interoperable with Db/Da and B.

In order to arrive at a minimum set of parameters necessary to describe seismic hazard in subduction zones we suggest to further explore the variability of those parameters in B, which are not well known in nature, to define the sensitivity of simpler proxies and to aim at constraining their upper and lower bounds.

Acknowledgments
This study has been partially funded by the German Research Foundation (DFG) collaborative research center SFB1114 "Scaling Cascades in Complex Systems," project B01. F.C. received funding from the European Union's Horizon 2020 research and innovation program under the Marie Sklodowska-Curie grant agreement 658034 (AspSync). Y. Kaneko and three anonymous reviewers are thanked for their very valuable comments which helped in clarifying and focusing this paper. We thank Y. Kaneko and J. P Avouac for discussions and sharing their data to populate Figure 9a. We thank Kirsten Elger and GFZ Data Services for publishing the experimental data underlying this study. All data underlying this study are published open access in GFZ Data Services: https://doi.org/10.5880/GFZ.4.1.2019.005.

References

Adam, J., Oncken, O., Kukowski, N., Lohrmann, J., Hoth, S., Urai, J. L., et al. (2005). Shear localisation and strain distribution during tectonic faulting—New insights from granular-flow experiments and high-resolution optical image correlation techniques. *Journal of Structural Geology*, *27*(2), 283–301. https://doi.org/10.1016/j.jsg.2004.08.008

Bilek, S. L., & Lay, T. (2018). Subduction zone megathrust earthquakes. *Geosphere*, *14*(4), 1468–1500. https://doi.org/10.1130/GES01608.1

Bookhagen, B., Echtler, H. P., Melnick, D., Strecker, M. R., & Spencer, J. Q. G. (2006). Using uplifted Holocene beach berms for paleo-seismic analysis on the Santa María Island, south-central Chile. *Geophysical Research Letters*, *33*, L15302. https://doi.org/10.1029/2006GL026734

Caniven, Y., Dominguez, S., Soliva, R., Cattin, R., Peyret, M., Marchandon, M., et al. (2015). A new multilayered visco-elasto-plastic experimental model to study strike-slip fault seismic cycle. *Tectonics*, *34*, 232–264. https://doi.org/10.1002/2014TC003701

Caniven, Y., Dominguez, S., Soliva, R., Peyret, M., Cattin, R., & Maerten, F. (2017). Relationships between along-fault heterogeneous normal stress and fault slip patterns during the seismic cycle: Insights from a strike-slip fault laboratory model. *Earth and Planetary Science Letters*, *480*, 147–157. https://doi.org/10.1016/j.epsl.2017.10.009

Comte, D., & Pardo, M. (1991). Reappraisal of great historical earthquakes in the northern Chile and southern Peru seismic gaps. *Natural Hazards*, *4*, 23–44.

Corbi, F., Funiciello, F., Brizzi, S., Lallemand, S., & Rosenau, M. (2017). Control of asperities size and spacing on seismic behavior of subduction megathrusts. *Geophysical Research Letters*, *44*, 8227–8235. https://doi.org/10.1002/2017GL074182

Corbi, F., Funiciello, F., Moroni, M., van Dinther, Y., Mai, P. M., Dalguer, L. A., & Faccenna, C. (2013). The seismic cycle at subduction thrusts: 1. Insights from laboratory models. *Journal of Geophysical Research: Solid Earth*, *118*, 1483–1501. https://doi.org/10.1029/2012JB009481

Franzke, C., O'Kane, T., Monselesan, D., Risbey, J., & Horenko, I. (2015). Systematic attribution of secular southern hemispheric circulation trends with observational forcing data. *Nonlinear Processes in Geophysics*, *22*, 513–525. https://doi.org/10.5194/npg-22-513-2015

Goldfinger, C., Nelson, C. H., Johnson, J. E., & The Shipboard Scientific Party (2003). Holocene earthquake records from the Casca-dia subduction zone and northern San Andreas fault based on precise dating of offshore turbidites. *Annual Review of Earth and Planetary Sciences*, *31*, 555–577. https://doi.org/10.1146/annurev.earth.31.100901.141246

Hayes, G. P. (2017). The finite kinematic rupture properties of great-sized earthquakes since 1990. *Earth and Planetary Science Letters*, *468*, 94–100. https://doi.org/10.1016/j.epsl.2017.04.003

Horenko, I. (2009). On robust estimation of low-frequency variability trends in discrete Markovian sequences of atmospheric circulation patterns. *Journal of the Atmospheric Sciences*, *66*(11), 1941–1954.

Horenko, I. (2010). Finite element approach to clustering of multidimensional time series. *SIAM Journal on Scientific Computing*, *32*(1), 62–83. https://doi.org/10.1137/080715962

Hubbert, M. K. (1937). Theory of scale models as applied to the study of geological structures. *Geological Society of America Bulletin*, *48*, 459–1520.

Kaiser, O., Igdalov, D., & Horenko, I. (2015). Statistical regression analysis of threshold excesses with systematically missing covariates. *SIAM Multiscale Modeling & Simulation (SIAM MMS)*, *13*(2), 594–613. https://doi.org/10.1137/140972184

Kaneko, Y., Avouac, J. P., & Lapusta, N. (2010). Towards inferring earthquake patterns from geodetic observations of interseismic coupling. *Nature Geoscience*, *3*(5), 363–369. https://doi.org/10.1038/ngeo843

King, G. C. P., Stein, R. S., & Lin, J. (1994). Static stress changes and the triggering of earthquakes. *Bulletin of the Seismological Society of America*, *84*(3), 935–953.

Kuehn, N. M., Hainzl, S., & Scherbaum, F. (2008). Non-Poissonian earthquake occurrence in coupled stress release models and its effect on seismic hazard. *Geophysical Journal International*, *174*, 649–658. https://doi.org/10.1111/j.1365-246X.2008.03835.x

Lay, T., & Wallace, T. C. (1995). In R. Dmoswska & J. R. Holton (Eds.), *Modern global seismology*, *International Geophysics Series* (Vol. 58). San Diego: Academic Press.

Li, S., Moreno, M., Bedford, J., Rosenau, M., & Oncken, O. (2015). Revisiting viscoelastic effects on interseismic deformation and locking degree: A case study of the Peru-North Chile subduction zone. *Journal of Geophysical Research: Solid Earth*, *120*, 4522–4538. https://doi.org/10.1002/2015jb011903

Lin, J., & Stein, R. S. (2004). Stress triggering in thrust and subduction earthquakes and stress interaction between the southern San Andreas and nearby thrust and strike-slip faults. *Journal of Geophysical Research*, *109*, B02303. https://doi.org/10.1029/2003JB002607

Metzner, P., Putzig, L., & Horenko, I. (2012). Analysis of persistent non-stationary time series and applications. *Communications in Applied Mathematics and Computational Science (CAMCoS)*, *7*(2), 175–229.

Moreno, M., Melnick, D., Rosenau, M., Bolte, J., Klotz, J., Echtler, H., et al. (2011). Heterogeneous plate locking in the South–Central Chile subduction zone: Building up the next great earthquake. *Earth and Planetary Science Letters*, *305*(3–4), 413–424. https://doi.org/10.1016/j.epsl.2011.03.025

Moreno, M., Rosenau, M., & Oncken, O. (2010). 2010 Maule earthquake slip correlates with pre-seismic locking of Andean subduction zone. *Nature*, *467*(7312), 198–202. https://doi.org/10.1038/nature09349

Moreno, M. S., Bolte, J., Klotz, J., & Melnick, D. (2009). Impact of megathrust geometry on inversion of coseismic slip from geodetic data: Application to the 1960 Chile earthquake. *Geophysical Research Letters*, *36*, L16310. https://doi.org/10.1029/2009GL039276

Okada, Y. (1985). Surface deformation due to shear and tensile faults in a half-space. *Bulletin of the Seismological Society of America*, *75*(4), 1135–1154.

Okada, Y. (1992). Internal deformation due to shear and tensile faults in a half-space. *Bulletin of the Seismological Society of America*, *82*(2), 1018–1040.

O'Kane, T., Risbey, J., Monselesan, D., Horenko, I., & Franzke, C. (2016). On the dynamics of persistent states and their secular trends in the waveguides of the southern hemisphere troposphere. *Climate Dynamics*, *46*(11–12), 3567–3597. https://doi.org/10.1007/s00382-015-2786-8

Oleskevich, D. A., Hyndman, R. D., & Wang, K. (1999). The updip and downdip limits to great subduction earthquakes: Thermal and structural models of Cascadia, south Alaska, SW Japan, and Chile. *Journal of Geophysical Research*, *104*(B7), 14,965–14,991. https://doi.org/10.1029/1999JB900060

Pipping, E., Kornhuber, R., Rosenau, M., & Oncken, O. (2016). On the efficient and reliable numerical solution of rate-and-state friction problems. *Geophysical Journal International*, *204*(3), 1858–1866. https://doi.org/10.1093/gji/ggv512

Ramberg, H. (1967). *Gravity, deformation and the Earth's crust*. London: Academic Press.

Risbey, J., O'Kane, T., Monselesan, D., Franzke, C., & Horenko, I. (2015). Metastability of Northern Hemisphere teleconnection modes. *Journal of the Atmospheric Sciences*, *72*, 35–54. https://doi.org/10.1175/JAS-D-14-0020.1

Rosenau, M., Corbi, F., & Dominguez, S. (2017). Analogue earthquakes and seismic cycles: Experimental modelling across timescales. *Solid Earth*, *8*(3), 1–65. https://doi.org/10.5194/se-8-597-2017

Rosenau, M., Horenko, I., Corbi, F., Rudolf, M., Kornhuber, R., Oncken, O. (2019): Supplement to "Synchronization of great subduction megathrust earthquakes: Insights from scale model analysis", GFZ Data Services. https://doi.org/10.5880/GFZ.4.1.2019.005

Rosenau, M., Lohrmann, J., & Oncken, O. (2009). Shocks in a box: An analogue model of subduction earthquake cycles with application to seismotectonic forearc evolution. *Journal of Geophysical Research*, *114*, B01409. https://doi.org/10.1029/2008jb005665

Rosenau, M., Nerlich, R., Brune, S., & Oncken, O. (2010). Experimental insights into the scaling and variability of local tsunamis triggered by giant subduction megathrust earthquakes. *Journal of Geophysical Research*, *115*, B09314. https://doi.org/10.1029/2009jb007100

Rosenau, M., & Oncken, O. (2009). Fore-arc deformation controls frequency-size distribution of megathrust earthquakes in subduction zones. *Journal of Geophysical Research*, *114*, B10311. https://doi.org/10.1029/2009jb006359

Rudolf, M., Boutelier, D., Rosenau, M., Schreurs, G., & Oncken, O. (2016). Rheological benchmark of silicone oils used for analog modeling of short- and long-term lithospheric deformation. *Tectonophysics*, *666*. https://doi.org/10.1016/j.tecto.2015.11.028

Ruff, L. J. (1996). Large earthquakes in subduction zones: Segment interaction and recurrence times. In G. E. Bebout, D. W. Scholl, S. H. Kirby, & J. P. Platt (Eds.), *Subduction top to bottom* (pp. 91–104). Washington, DC: American Geophysical Union.

Scholz, C. H. (1998). Earthquakes and friction laws. *Nature*, *391*, 37–42. https://doi.org/10.1038/34097

Scholz, C. H. (2010). Large earthquake triggering, clustering, and the synchronization of faults. *Bulletin of the Seismological Society of America*, *100*(3), 901–909. https://doi.org/10.1785/0120090309

Shearer, P. M., & Stark, P. B. (2012). Global risk of big earthquakes has not recently increased. *Proceedings of the National Academy of Sciences of the United States of America*, *109*(3), 717–721. https://doi.org/10.1073/pnas.1118525109

Shreve, R. L., & Cloos, M. (1986). Dynamics of sediment subduction, melange formation, and prism accretion. *Journal of Geophysical Research*, *91*, 10,229–10,245. https://doi.org/10.1029/JB091iB10p10229

Sykes, L. R., & Menke, W. (2006). Repeat times of large earthquakes: Implications for earthquake mechanics and long-term prediction. *Bulletin of the Seismological Society of America*, *96*(5), 1569–1596. https://doi.org/10.1785/0120050083

Toda, S., & Stein, R. S. (2002). Response of the San Andreas fault to the 1983 Coalinga-Nuñez Earthquakes: An application of interaction-based probabilities for Parkfield. *Journal of Geophysical Research*, *107*(B6), 2126. https://doi.org/10.1029/2001JB000172

Toda, S., Stein, R. S., Sevilgen, V., & Lin, J. (2011). Coulomb 3.3 graphic-rich deformation and stress-change software for earthquake, tectonic, and volcano research and teaching—User guide: U.S. Geological Survey Open-File Report 2011–1060, 63 p. Retrieved from https://pubs.usgs.gov/of/2011/1060

Vercauteren, N., & Klein, R. (2015). A clustering method to characterize intermittent bursts of turbulence and interaction with submeso-scopic motions in the stable boundary layer. *Journal of the Atmospheric Sciences*, *72*, 1504–1517. https://doi.org/10.1175/JAS-D-14-0115.1